# Radiation damage in protein crystals is reduced with a micron-sized X-ray beam

Ruslan Sanishvili[a], Derek W. Yoder[a], Sudhir Babu Pothineni[a], Gerd Rosenbaum[b], Shenglan Xu[a], Stefan Vogt[c], Sergey Stepanov[a], Oleg A. Makarov (Олег Макаров)[a], Stephen Corcoran[a], Richard Benn[a], Venugopalan Nagarajan[a], Janet L. Smith[a,d], and Robert F. Fischetti[a,1]

[a]National Institute of General Medical Sciences and National Cancer Institute Collaborative Access Team, Biosciences Division, Argonne National Laboratory, Argonne, IL 60439; [b]Department of Biochemistry and Molecular Biology, University of Georgia, Athens, GA 30602; [c]X-Ray Science Division, Argonne National Laboratory, Argonne, IL 60439; and [d]Life Sciences Institute, Department of Biological Chemistry, University of Michigan, Ann Arbor, MI 48109

Edited by Douglas C. Rees, Howard Hughes Medical Institute, California Institute of Technology, Pasadena, CA, and approved February 23, 2011 (received for review November 30, 2010)

**Radiation damage is a major limitation in crystallography of biological macromolecules, even for cryocooled samples, and is particularly acute in microdiffraction. For the X-ray energies most commonly used for protein crystallography at synchrotron sources, photoelectrons are the predominant source of radiation damage. If the beam size is small relative to the photoelectron path length, then the photoelectron may escape the beam footprint, resulting in less damage in the illuminated volume. Thus, it may be possible to exploit this phenomenon to reduce radiation-induced damage during data measurement for techniques such as diffraction, spectroscopy, and imaging that use X-rays to probe both crystalline and noncrystalline biological samples. In a systematic and direct experimental demonstration of reduced radiation damage in protein crystals with small beams, damage was measured as a function of micron-sized X-ray beams of decreasing dimensions. The damage rate normalized for dose was reduced by a factor of three from the largest (15.6 μm) to the smallest (0.84 μm) X-ray beam used. Radiation-induced damage to protein crystals was also mapped parallel and perpendicular to the polarization direction of an incident 1-μm X-ray beam. Damage was greatest at the beam center and decreased monotonically to zero at a distance of about 4 μm, establishing the range of photoelectrons. The observed damage is less anisotropic than photoelectron emission probability, consistent with photoelectron trajectory simulations. These experimental results provide the basis for data collection protocols to mitigate with micron-sized X-ray beams the effects of radiation damage.**

microcrystallography | synchrotron radiation

The brilliance of synchrotron radiation from undulator devices on third-generation sources has been an enormous boon to crystallography of biological macromolecules. The high flux density and low divergence of undulator beams led to a rapid decrease in the minimum crystal size and minimum beam size that can yield usable diffraction data (1–4). However, the resulting decrease in diffracting volume necessitates an increase in X-ray exposure per unit sample volume, increasing radiation damage and severely compromising the substantial benefits of brilliant undulator sources. Thus, there is considerable interest in understanding the mechanism and spatial extent of X-ray–induced damage to crystals of biological macromolecules.

Diffraction experiments are typically performed at cryotemperatures (approximately 100 K) to prevent the diffusion of free radicals, which are a major source of damage in crystals exposed to X-rays at higher temperatures (5), but cryocooling does not eliminate X-ray damage. Many experimental approaches to circumventing the effects of radiation damage have been investigated (6–10) but have not yet yielded a breakthrough result. Zero-dose diffraction intensities have been extrapolated from measured values by mathematical modeling (7–9). The effects of radiation damage have also been exploited for crystallographic phase determination (10–16). Nevertheless, it remains a goal to eliminate or minimize structural damage in order to avoid artifacts in the resulting structures and erroneous mechanistic interpretations.

Of several potential sources of X-ray–induced damage to cryocooled samples at typical energies (6–18 keV), the main contributor is thought to be energy deposited by photoelectrons that are generated by the interaction of incident X-ray photons with the sample. The photoelectrons deposit energy as they traverse the sample and are scattered by atoms. The energy deposited as a function of distance increases as the photoelectron energy decreases from successive interactions. Photoelectrons are emitted preferentially along the polarization direction of the X-ray beam, leading to an expectation of anisotropy in photoelectron emission (17) and therefore in photoelectron-induced damage. Monte Carlo simulations of photoelectron trajectories predicted that the greatest energy deposition in the photoelectron flight path was a few microns from the photoelectron origin, and that the photoelectrons would escape the illuminated crystal volume if the crystal (18) or the beam (19) were small relative to the photoelectron path length. Thus, there is a potential for reducing radiation damage if the incident X-ray beam size is decreased beyond the microbeams now in use, which are as small as 5–10 μm (20–22). Photoelectron transfer of energy out of the beam footprint causing "penumbral damage" is well known in radiology and has been observed in studies with high-energy (MeV) X-rays (23). Other sources of energy deposition outside the illuminated volume such as Compton scattering and Auger emission can be ruled out because both Compton and Auger electrons are of low average energy (<1 keV) and have a very short range (<100 nm) in the protein medium.

Here, we investigate the hypothesis that energy can be transferred out of the footprint of a micron-sized beam on a protein crystal, thereby reducing radiation damage within the illuminated volume relative to the situation with a larger beam. We also measure the spatial extent of radiation damage outside the beam footprint and test whether the damage is distributed anisotropically relative to the polarization direction.

Author contributions: R.S., G.R., J.L.S., and R.F.F. designed research; R.S., D.W.Y., and R.F.F. performed research; S.B.P., S.X., S.V., S.S., O.A.M., S.C., R.B., and V.N. contributed new reagents/analytic tools; R.S., D.W.Y., J.L.S., and R.F.F. analyzed data; and R.S., G.R., J.L.S., and R.F.F. wrote the paper.

The authors declare no conflict of interest.

This article is a PNAS Direct Submission.

[1]To whom correspondence should be addressed. E-mail: rfischetti@anl.gov.

This article contains supporting information online at www.pnas.org/lookup/suppl/doi:10.1073/pnas.1017701108/-/DCSupplemental.

## Results

**Radiation Damage Varies with Beam Size.** If the primary source of radiation damage in cryocooled protein crystals is the energy deposited by photoelectrons, then the fraction of the energy of the absorbed photon that is deposited in the beam footprint will decrease as beam size is decreased below the length scale of photoelectron energy deposition. We sought to detect this effect using an 18.5-keV X-ray beam of six sizes ranging from 15.6- to 0.84-μm average diameter, achieved using two different optical configurations of beamline 23ID-B at the Advanced Photon Source (Figs. S1 and S2; Tables S1 and S2). To evaluate damage, repeated diffraction images were recorded from a fixed position on a large lysozyme crystal, using an unexposed volume for each beam size. Damage was monitored as the decrease of the sum of intensities of all Bragg peaks in each image, normalized to the total intensity in the first image. For each diffraction image, the physical and chemical properties of the sample and the intensity, size, and shape of the X-ray beam were used to calculate the dose, assuming no photoelectrons escaped the illuminated volume (24). We designate this as the "calculated dose." For each beam size, the normalized intensity decreased linearly with increasing dose, indicative of radiation damage (Fig. 1*A*). However, the damage rate (slope of the intensity vs. calculated dose curve) changed with beam size for beams up to about 10 μm. The damage rate for the largest beam used (15.6 μm) is comparable to measurements with a 100-μm beam (25). The decreased rate with decreasing beam size clearly indicates the transfer of deposited energy out of the illuminated volume. To further illustrate the beam-size effect, the radiation damage per calculated dose was determined as a function of beam size (Fig. 1*B*). The damage rate normalized for the calculated dose was reduced by a factor of three from the largest (15.6 μm) to the smallest (0.84 μm) X-ray beam used. The rate of energy deposited per mass of irradiated crystal dropped sharply for beam sizes less than 5 μm. These results are a direct experimental demonstration of reduced radiation damage in the volume of a protein crystal illuminated with micron-sized, hard X-ray (keV) beams.

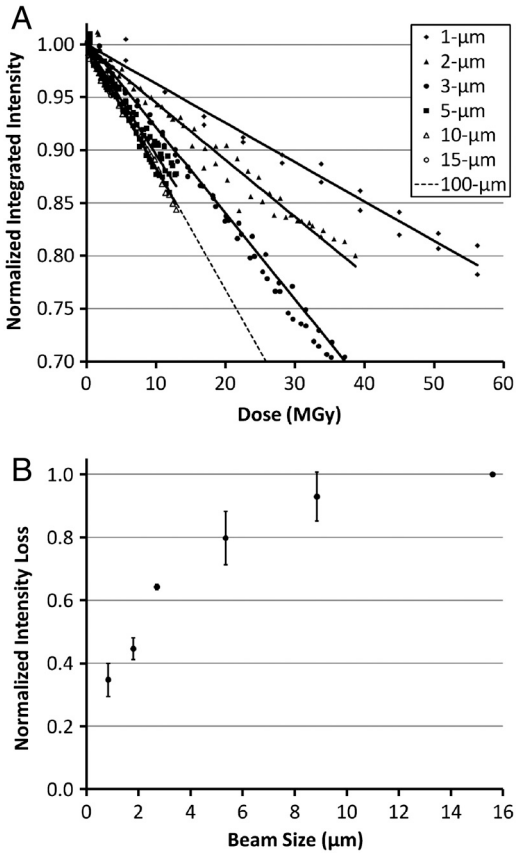


**Fig. 1.** Damage per calculated dose as a function of beam size for 18.5-keV X-rays. (*A*) Normalized sum of all diffracted intensities as a function of calculated dose for data collected with average beam diameters of 0.84, 1.81, 2.71, 5.35, 8.85, and 15.6 μm. Doses were calculated using RADDOSE (24). The dotted line represents an assumed linear rate of damage for which the intensity decays to 50% at a dose of $4.3 \times 10^7$ Gy, as measured with a 100-μm beam (25). (*B*) Damage rate as a function of beam diameter. The slope of each curve in *A* was normalized by the value at 15.6 μm. The beam size is the average of the horizontal and vertical beam sizes. The data were collected by rotating the crystal through 1° about the horizontal axis; and therefore a small correction was applied to account for the swept volume (Table S3). Error bars represent $\pm 1\sigma$ of multiple experiments.

**Spatial Extent of Radiation Damage.** We next investigated how far radiation damage extends beyond the beam footprint in a protein crystal. The goal was to record with high spatial resolution the damage distribution around a central "burn" position. A single position on a large lysozyme crystal was subjected to several burn doses of radiation. Each burn dose was preceded and followed by probe measurements at several positions offset from the burn position by steps of $1.00 \pm 0.05$ μm in directions parallel (horizontal) or perpendicular (vertical) to the polarization direction (Fig. 2*A*). Damage was monitored as the fractional change in total integrated diffraction intensity ($\Delta_i$) at the probe positions. By this measure, damage extended to at least 9 μm from the burn position (Fig. S3*A*). However, two sources of unintentional damage contributed to this result. First, the probe measurements themselves were a source of damage, which we sought to remove from the data. In each experiment at each probe position, the measured fractional decay value ($\Delta_i$) was corrected for probe damage by subtraction of the fractional decay per image calculated from a series of successive images measured with the same parameters as the probe images (Fig. S4). This probe-damage correction reduced the baseline of damage at all probe positions, but again residual damage persisted to 9 μm, the farthest distance probed from the burn position (Fig. S3*B*).

A second source of unintentional damage was from beams at neighboring probe positions. Adjacent probes directly overlapped because the width of the probe beam was comparable to the spacing between probe positions. Additionally, photoelectrons escaping from neighboring probes may deposit energy outside the footprint of the 1-μm probe beam. These considerations were the impetus for using the isolated-probe protocol (Fig. 2*B*), which does not suffer from neighbor effects. The fractional damage for experiments using the isolated-probe protocol was significantly reduced at remote positions from the burn position compared to contiguous-probe experiments (Fig. S3*A* vs. Fig. S3*C*). After probe-damage correction, data from the isolated-probe experiments showed no evidence of damage at the probe positions most distant from the burn position (Fig. S3*D*). Thus, the

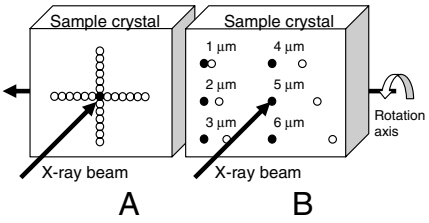


**Fig. 2.** Experimental design to measure the spatial extent of radiation damage. (*A*) Contiguous-probe protocol. Probe measurements (open circles) were recorded at each position in the pattern before and after each burn dose at the burn position (filled circle). (*B*) Isolated-probe protocol. The probe measurements (open circles) were not contaminated by neighboring probe measurements because a separate burn position (filled circles) was used for each probe position.

isolated-probe protocol allowed a direct measurement of the damage distribution. Using the isolated-probe protocol, 15 experiments on 8 crystals were carried out, and the results for each probe position at each energy were averaged.

The maps of the spatial extent of radiation damage in the horizontal and vertical directions for 15.1-keV and 18.5-keV X-rays (Fig. 3) displayed a high degree of symmetry, demonstrating the accuracy and reproducibility of sample motion during multiple probe-burn-probe sequences, consistent with the $<100$ nm measured reproducibility, accuracy, and stability of the mechanical motions in the experimental setup. The plots for successive probe-burn experiments showed an increase of damage with accumulated dose at the same position. The observed damage profile was greatest at the center and decayed monotonically to zero within measurement error at a distance of about 4 μm for all doses at the two incident X-ray energies. The average half-width at half-maximum (HWHM) of the damage profile at 15.1 keV was $1.83 \pm 0.15$ μm horizontally and $1.54 \pm 0.16$ μm vertically, using a beam with full-width at half-maximum (FWHM) dimensions 1.16 μm × 1.18 μm (horizontally × vertically, H × V) (Fig. 3 *A* and *C*). However, despite the small beam width, the 15.1-keV burn beam significantly overlapped the first probe position and partially overlapped the second. To more accurately measure the width of the damage distribution, a finer probe beam of dimensions 0.88 μm × 0.80 μm H × V (FWHM) was used. The X-ray energy also was increased to 18.5 keV to increase the photoelectron range owing to the reduced stopping power of the protein medium at higher energies. The resulting HWHM was $1.84 \pm 0.15$ μm horizontally and $1.21 \pm 0.03$ μm vertically (Fig. 3 *B* and *D*). Accounting for beam size, the width of the damage distribution increased by 3% horizontally and decreased by 20% vertically as the X-ray energy was increased from 15.1 to 18.5 keV. The combination of fine focus, high energy, and isolated-probe protocol led to nonoverlapping burn and probe beams at 18.5 keV (except for partial overlap with the 1-μm probe position), which allowed direct measurement of the magnitude of damage.

The horizontal and vertical damage profiles for the maximum dose used in the experiment at 18.5 keV were each averaged about the origin in order to compare them with the best-fit Gaussian profile of the beam (Fig. 4). The damage profiles are slightly anisotropic with a lower magnitude of damage at a given distance from the burn center in the vertical than in the horizontal direction. The spatial extent of the damage exceeded the beam width by a factor of 4.2 in the horizontal and 3.0 in the vertical direction, demonstrating penumbral damage. This is consistent with results on the beam-size dependence of damage rate (Fig. 1).

**Monte Carlo Simulations.** To reconcile our experimental results with photoelectron emission theory, photoelectron trajectories were calculated to model the distribution and spread of photoelectrons. The X-ray beam from Advanced Photon Source Undulator A was 99% transversely polarized in the horizontal plane, resulting in an anisotropic photoelectron emission probability. The photoelectric cross-section for s-shell electrons is typically an order of magnitude greater than for other shells and is the source of over 95% of the photoelectric cross-section for low-Z elements. Thus, the probability of ejection of a photoelectron is symmetric about the polarization vector, and is approximately proportional to $\cos^2(\theta)d\Omega$, where $\theta$ is the angle between the directions of polarization and emission and $d\Omega$ is the solid angle (17). A photoelectron is deflected randomly by each collision, and the average deflection angle increases with decreasing energy of the electron. Therefore, the trajectories of the photoelectrons spread with increasing distance from the origin.

Previous simulations (18) considered only photoelectron trajectories that originated from a single point with an initial vector along the polarization direction ($\theta = 0°$). For a more realistic model of the distribution of energy deposited by photoelectrons, Monte Carlo simulations of the photoelectron trajectories were

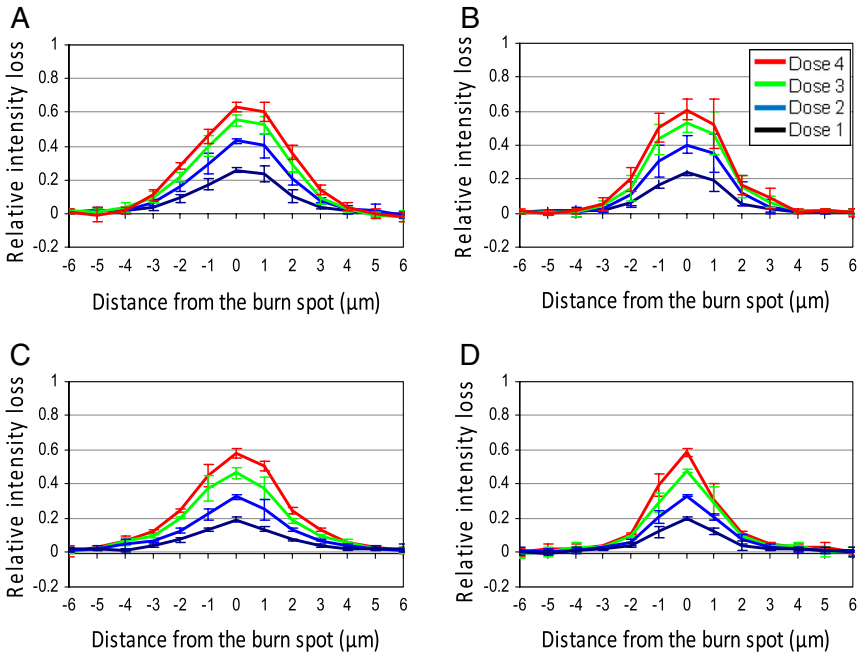


**Fig. 3.** Spatial extent of radiation damage in lysozyme crystals. Fractional loss of total integrated reflection intensity as a function of distance from the burn position in the horizontal and vertical directions for four probe-burn-probe sequences at 15.1 keV (beam size: 1.16 μm FWHM horizontal; 1.18 μm vertical) and 18.5 keV (0.88 μm horizontal; 0.80 μm vertical). The dose was increased by equal increments for the damage distribution curves in the order black, blue, green, and red. (*A*) Damage in the horizontal direction at 15.1 keV. (*B*) Damage in the horizontal direction at 18.5 keV. (*C*) Damage in the vertical direction at 15.1 keV. (*D*) Damage in the vertical direction at 18.5 keV. The damage is greatest at the center and decays monotonically to zero (within experimental error) by 4 μm from the beam center for both energies. Error bars represent $\pm 1\sigma$ of multiple experiments.

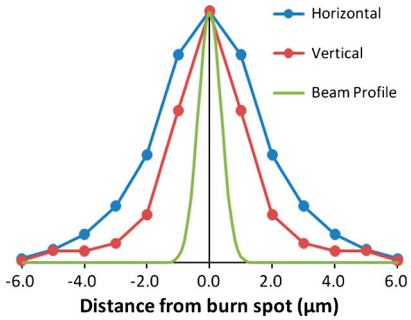


**Fig. 4.** Comparison of spatial extent of radiation damage and the beam size at 18.5 keV. The blue and red curves show the damage distribution in the horizontal and vertical directions, respectively. The data from the red curves (maximum dose) in Fig. 3 *B* and *D* were averaged about the origin and then normalized at the origin. The widths of the damage distributions are significantly larger than the width of the X-ray beam (green line, average FWHM = 0.84 μm), and are slightly anisotropic.

conducted using 2,000 points within a 1-μm-diameter beam as the source for trajectories that initially were parallel to the polarization vector at photoelectron energies of 14.4 keV and 17.8 keV (Fig. 5*A*). These energies correspond to 15.1- and 18.5-keV X-ray photons, respectively, given the 0.7-keV average binding energy of s-shell electrons. As expected, the trajectories at the higher energy penetrated the sample further and spread over a larger volume than did those at the lower energy.

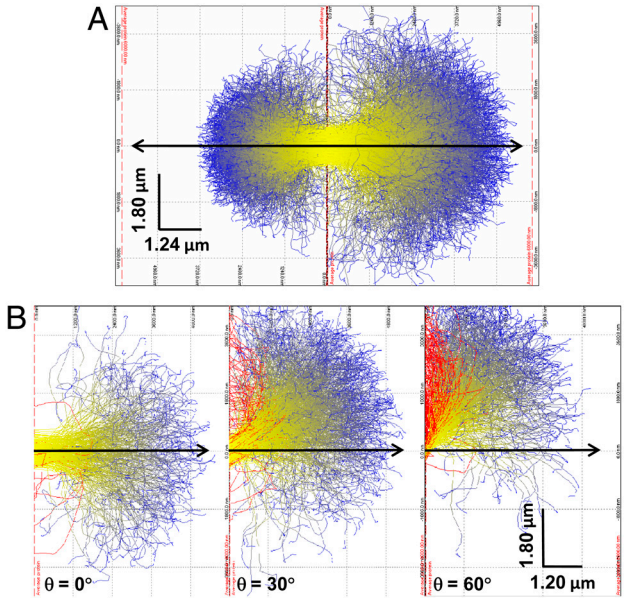


**Fig. 5.** Monte Carlo simulation of photoelectron trajectories. (*A*) 2,000 trajectories for photoelectrons of energy 14.4 keV (*Left*) and 17.8 keV (*Right*) in a protein crystal. Trajectories originated at $\theta = 0°$ (parallel to the polarization vector, black arrow) and simulate a 1-μm diameter X-ray beam directed into the viewing plane. The 3D mushroom-like distribution is projected onto a horizontal plane and colored from yellow to blue with decreasing photoelectron energy. The spatial extent of the trajectories is considerably shorter for the 14.4-keV electrons than for the 17.8-keV electrons. Only one half of each symmetric distribution is shown. (*B*) Trajectories of photoelectrons emitted at 0° (*Left*), 30° (*Middle*), and 60° (*Right*) relative to the polarization vector. The number of electrons in the simulation was proportional to the probability of ejection within azimuth angles between 0° and 20° for the 0° beam angle simulation, 20° and 45° for the 30° simulation, and 45° and 75° for the 60° simulation. Actual trajectories are distributed isotropically around the polarization vector for the given azimuth angle range. The strong curvature of the photoelectron trajectories at lower energy toward the end of their travel results in some backscatter (red).

The spatial distribution of the radiation damage about the burn position depends on the true photoelectron emission angle and on the scattering of the photoelectron as it traverses the sample. The full distribution was approximated by carrying out simulations at three emission angles, each weighted by the solid angle for a given $\Delta\theta$ angular range about the emission angle (Fig. 5*B*). These projections indicate that as the emission angle of the initial trajectory increases from $\theta = 0°$ to 30° to 60°, a significant fraction of the photoelectrons scatter in the vertical direction and deposit energy perpendicular to the polarization direction. These simulations are consistent with our observation that the damage distribution is weakly anisotropic; i.e. the magnitude of damage at a given distance from the burn center is only slightly less in the direction perpendicular than in the direction parallel to the polarization direction (Fig. 4).

## Discussion

Our experiments with a micron-sized probe beam tracked radiation damage as the loss of intensities in Bragg peaks from cryocooled lysozyme crystals. Radiation damage increased linearly with dose for each beam size studied at 18.5 keV (Fig. 1*A*). The decay rate (loss of diffracted intensity per calculated dose) for the largest beam (15.6 μm) was in good agreement with previous measurements using a 100-μm beam (25). However, as the beam size was decreased from 15.6 to 0.84 μm, the decay rate decreased, indicating a reduction of damage per calculated dose within the beam footprint and implying the transfer of some energy out of the illuminated volume. In another set of experiments with an approximately 1-μm beam, the spatial distribution of the radiation damage (Fig. 3) indicated that damage was greatest at the beam center and decayed monotonically to zero within experimental error at a distance of about 4 μm for all doses at the two incident X-ray energies. These results are a clear demonstration of damage outside the beam footprint in cryocooled protein crystals, providing direct evidence of photoelectron escape from the illuminated volume.

The measurement of decay as a function of beam size (Fig. 1*B*) is direct evidence that radiation damage within the diffracting volume can be reduced by reducing the size of the X-ray beam, as proposed by Nave and Hill (18). Several observations of greater than anticipated robustness of very small (<10 μm) crystals (26, 27) or of larger crystals probed with very small (<10 μm) beams (3, 28, 29) have been attributed to photoelectron escape from the illuminated volume and provided indirect evidence of this phenomenon. In our direct measurements, the sample survivability was increased by a factor of three over the range of beam sizes studied with 18.5-keV incident X-rays. Others have calculated as high as a 10-fold small-beam enhancement, defined as the ratio of the elastic scattering to inelastic scattering cross-sections, based on the assumption that photoelectrons transport energy out of micron-sized crystals or out of the footprint of micron-sized beams (3, 19).

In typical crystallographic experiments with beams larger than 15 μm and X-ray energies near 12 keV, the damage transferred out of the beam footprint is negligible. Common calculations of dose (energy deposited per unit sample mass) for a specific experiment (sample content and size; photon energy; beam intensity, size, and shape; and exposure time) assume all the energy of the absorbed photons is deposited within the illuminated volume and are well adapted to the typical situation (24). However, for small beams, some energy escapes the beam footprint and results in a penumbral dose in the volume surrounding the beam footprint. This effect was observed as an intensity loss at the probe positions in our experiments (Fig. 3). Thus, dose calculations for small beams need revision to properly describe the actual dose within the diffracting volume. Similarly, dose-based estimates of the minimum crystal size required to obtain useful diffraction data (2) need to be revised to include photoelectron escape.

The observed damage profile places an upper limit on the range of the photoelectron from the beam center for the given incident X-ray energy and beam size. The photoelectron range is of great practical importance in microcrystallography because it permits calculation of the minimum sample translation required to expose an undamaged crystal volume to the beam. The intrinsic rms width of the photoelectron-induced radiation damage is estimated to be $\sigma_{pe} = 1.52$ μm in the horizontal and 0.97 μm in the vertical directions at 18.5 keV, based on deconvolution of the observed beam width ($\sigma_b = 0.37$ μm × 0.34 μm, H × V) from the observed width of the damage ($\sigma_d = 1.56$ μm× 1.03 μm, H × V), assuming a Gaussian profile for the damage distribution. Thus, a sample translation of 4.0 μm would expose a fresh volume to a 1-μm beam at 18.5 keV, as would translations of 5.2 μm for a 2-μm beam, 6.5 μm for a 3-μm beam, 9.5 μm for a 5-μm beam, and 17.5 μm for a 10-μm beam (based on an overall $4\sigma$ separation).

The spatial extent of the damage exceeded the beam size by a factor of 3.0 in the vertical direction and 4.2 in the horizontal for 18.5-keV incident X-rays (Fig. 4). The horizontal damage distribution was negligibly different at 15.1 and 18.5 keV because of the offsetting experimental factors of a larger beam at 15.1 keV and a greater photoelectron range at 18.5 keV. In contrast, the vertical distribution was narrower at 18.5 keV than at 15.1 keV, most likely due to the reduced probability that a photoelectron will scatter back to the vertical axis at the higher energy (Fig. 5). Our measured results are in good agreement with Monte Carlo simulations of photoelectron trajectories in a medium of average electron density equivalent to a typical protein crystal, considering the approximations of a homogeneous, noncrystalline medium, and the planar geometry of the simulations (18) (Fig. 5*A*). Our measurement of a 4-μm spatial extent of damage with a nearly circular beam of width 0.84 μm (FWHM) and of energy 18.5 keV (Fig. 3) differs from an estimate of photoelectron penetration depth of 1.5 μm, based on data from a line-focus beam with a width of 2.47 μm (FWHM) and an energy of 18.6 keV (30). The line-focus experiment used a protocol similar to our contiguous-probe approach yielding similar raw data (Fig. S3*A*). Our isolated protocol, which is free of probe-damage artifacts, provides a direct measure of the photoelectron penetration depth.

For a photoelectron ejected from an atom in a crystal, the energy deposited as a function of distance traveled is low at first and increases rapidly as the photoelectron scatters inelastically, losing energy with each collision until eventually it is recaptured. It was predicted that a 20-keV electron could travel a little farther than 4 μm (18) and that the energy deposition profile for 20-keV photons would have a peak at approximately 4 μm from the site of photoelectron ejection (31). However, the calculated profile is strongly dependent on the relative cross-sections of the sample and beam and on the solid angle of detection used in the calculations. No peak of any statistical significance was observed in our data other than the central peak. The monotonic decrease in damage with distance from the beam center (Fig. 3) is in better agreement with other calculations that employed a geometry more similar to our experimental conditions (3).

The increased range of photoelectrons with increasing incident X-ray energy is clear in the side-by-side Monte Carlo simulations for 1-μm-diameter beams with incident X-ray energies of 15.1 and 18.5 keV, in which the photoelectrons are ejected with an initial trajectory parallel to the polarization direction (Fig. 5*A*). The trajectories initially are straight, but they deviate significantly from the emission direction toward the end of their travel, resulting in a mushroom-shaped distribution. A more accurate representation of the spatial extent and distribution of energy deposition in protein crystals must include the angular distribution $[\cos^2(\theta)d\Omega]$ of the photoelectron emission probability. As the angle of the initial trajectory increases from 0 to 60°, the electron trajectories show an increasing probability of energy deposition perpendicular to the polarization direction; i.e., along the vertical axis (Fig. 5*B*). Our simulations with a 1-μm beam are consistent with our experimental observations that the degree of anisotropy of the distribution of damage in the horizontal and vertical directions is less than expected based on previous simulations (18).

Our measurements show that the crystal dimension in the direction parallel to the polarization vector need not be thin to exploit the photoelectron escape effect. If either the beam or the crystal is small, the photoelectron can escape the diffracting volume. Damaging photoelectrons will be generated in any nondiffracting part of the sample (crystal mounting solution) that is in the beam path, so it is important that the beam intercept only a volume that diffracts. It has been proposed that one or several line-focused beams (focused to micron dimensions in the horizontal direction and tens of microns in the vertical direction) could be used to take advantage of the photoelectron path length and anisotropic geometry of the emission probability to reduce radiation damage (30). However, our direct mapping of damage using a submicron, nearly circular probe beam shows substantial damage in both the vertical and horizontal directions at 18.5 keV, suggesting that calculations need revision to account for the observed low anisotropy and to accommodate more realistic experimental geometries. The observed anisotropy, although small, argues that a crystal rotation axis parallel to the beam polarization direction is optimal in data collection protocols that exploit photoelectron escape.

An incident X-ray energy greater than 18.5 keV would generate a higher-energy photoelectron, which would deposit a greater fraction of its energy outside the beam footprint than observed in our experiments. However, the Compton-scattering cross-section also increases with X-ray energy, resulting in more energy deposition within the illuminated volume of the crystal. Despite this increase, the Compton-scattering cross-section is considerably less than the photoelectric cross-section (32). By considering the competing photoelectron and Compton effects, an optimal energy for minimum radiation damage per dose was calculated to be between 20 and 40 keV for crystal or beam sizes between 1 and 15 μm (19). The 20–40 keV energy range should be explored to determine whether protocols based on photoelectron escape are practical for microcrystallography. Detectors optimized for this energy range may be needed to fully explore the potential of 20–40 keV X-ray beams.

We have shown that for cryocooled protein crystals, radiation damage per calculated dose of 18.5-keV X-rays decreased 3-fold as the beam size was decreased from 15.6 to 0.84 μm because some energy escaped the beam footprint. In addition, we mapped the spatial distribution of radiation damage about a 1-μm beam, showing that the extent was limited to approximately 4 μm and that the radius of the damage was 4-fold greater than the beam radius. These two observations strongly support the concept that photoelectrons carry energy out of the footprint of micron-sized beams, thereby reducing radiation damage within the illuminated volume. With even smaller samples or beams and/or higher X-ray energies, it may be possible to exploit this phenomenon to record diffraction, spectroscopic, or imaging data of higher quality with fewer artifacts from photoelectron-induced damage.

## Methods

The radiation damage experiments were performed on beamline 23-ID-B of the Advanced Photon Source, Argonne National Laboratory (33). The wide range of beam sizes required two different optical configurations (Fig. S1). Beam sizes between 5 and 15 μm with a nearly circular cross-section were achieved by using minibeam collimators (20) in combination with focusing mirrors (Table S1). For beam sizes less than 5 μm, circular Fresnel zone plate optics (34) were used to focus the beam at the sample position. The convergence angle of the beam at the sample position was quite small compared to

the sample rocking curve width, allowing all reflections to be fully resolved for all beam sizes and all samples used in these experiments (Table S2).

Total flux was monitored during the experiment with an "active" beamstop (35). Flux densities were derived from the measured beam profiles and the total flux (Table S1; see *SI Text* for details). Essential modifications were made to the experimental endstation instrumentation to achieve the desired approximately 0.1-μm stability, accuracy, and reproducibility of the beam position and sphere-of-confusion of the goniometry, which should be <10% of the beam or sample size (35). These parameters were verified using an optical autocollimator (LDS1000, Newport Corp.) with an objective lens (M Plan Apo 20×, Mitutoyo Corp.) to achieve approximately 50-nm resolution.

Diffraction measurements were made from tetragonal chicken egg-white lysozyme crystals with dimensions of 50–300 μm perpendicular to the beam and 30–60 μm along the beam. Crystals were mounted in MiTeGen micromounts (MiTeGen, LLC) to minimize the amplitude of vibrations in the stream of cold $N_2$ gas that maintained the crystals at 100 K during measurements. Decay was monitored as the change in the sum of intensities ($I$) of all Bragg reflections with $I/\sigma_I > 2$, including all partially and fully recorded reflections. Each measurement was a single diffraction image of rotation width 1.0°.

To measure radiation damage as a function of beam size, repeated diffraction images of 1° rotation range were recorded from a single position on the crystal until the total diffracted intensity decayed by at least 10–20%. When a crystal was sufficiently large, multiple experiments were conducted on that crystal by translating a fresh volume of the crystal into the beam. Based on preliminary measurements of the spatial extent of damage, for the 3-μm and smaller beam sizes the sample was translated at least 15 μm between experiments, and for the 5-μm and larger beams the sample was translated at least 30 μm. The dose calculated using RADDOSE (24) is based on a stationary illuminated volume. During the 1° crystal rotation, fresh volume was swept into the beam and exposed volume was swept out of the beam, and thus the calculated dose is overestimated. A swept-volume correction was applied to the damage rate normalized for the calculated dose shown in Fig. 1*B* (Table S3; see *SI Text*).

To measure the spatial extent of radiation damage, diffraction images were recorded with beams of dimensions 1.16 μm × 1.18 μm (H × V, FWHM) at 15.1 keV and 0.88 μm × 0.80 μm (H × V, FWHM) at 18.5 keV in a probe-burn-probe mode with burn and probe positions offset in the horizontal or vertical direction by a specified distance (Fig. 2). Burn-probe sequences were repeated until the total diffracted intensity decayed by more than 50%. Each burn dose comprised 10 successive diffraction images over the same angular range as the probe images. Two probe-burn-probe protocols were used. In the contiguous-probe approach (Fig. 2*A*), an initial probe image was recorded for all positions of the desired pattern, the crystal was then translated back to the origin and subjected to a burn dose, diffraction images were recorded again at all probe positions, and the process was repeated several times. In the isolated-probe approach (Fig. 2*B*), the pattern was composed from individual burn/probe pairs in which a spatially isolated probe-$(\text{burn-probe})_n$ sequence was performed for each distance. For each probe position, radiation damage was monitored as the fractional decay ($\Delta_i$) of the total diffracted intensity ($I$) and calculated for successive diffraction images as

$$\Delta_i = 1 - I_i/I_1, \qquad [1]$$

where $I_i$ and $I_1$ are the total diffracted intensities of the $i$th and initial images at the probe position, respectively. Diffraction images in the initial burn series of each experiment were used to correct decay curves for radiation damage caused by measurement of the probe images themselves. The fractional intensity loss per image in the initial burn series was taken as a measure of probe damage and subtracted from $\Delta_i$ to obtain a corrected fractional decay value.

**ACKNOWLEDGMENTS.** The authors thank Colin Nave, Elspeth Garman and Liz Duke for helpful discussions. The National Institute of General Medical Sciences and National Cancer Institute Collaborative Access Team is supported by the National Institute of General Medical Sciences (Y1-GM-1104) and the National Cancer Institute (Y1-CO-1020) of the US National Institutes of Health. Use of the Advanced Photon Source was supported by the US Department of Energy, Basic Energy Sciences, Office of Science, under Contract DE-AC02-06CH11357.

1. Nelson R, et al. (2005) Structure of the cross-beta spine of amyloid-like fibrils. *Nature* 435:773–778.
2. Holton JM, Frankel KA (2010) The minimum crystal size needed for a complete diffraction data set. *Acta Crystallogr D* 66:393–408.
3. Moukhametzianov R, et al. (2008) Protein crystallography with a micrometre-sized synchrotron-radiation beam. *Acta Crystallogr D* 64:158–166.
4. Sanishvili R, et al. (2008) A 7 μm mini-beam improves diffraction data from small or imperfect crystals of macromolecules. *Acta Crystallogr D* 64:425–435.
5. O'Neill P, Stevens DL, Garman EF (2002) Physical and chemical considerations of damage induced in protein crystals by synchrotron radiation: A radiation chemical perspective. *J Synchrotron Radiat* 9:329–332.
6. Murray J, Garman E (2002) Investigation of possible free-radical scavengers and metrics for radiation damage in protein cryocrystallography. *J Synchrotron Radiat* 9:347–354.
7. Diederichs K, McSweeney S, Ravelli RB (2003) Zero-dose extrapolation as part of macromolecular synchrotron data reduction. *Acta Crystallogr D* 59:903–909.
8. Diederichs K (2006) Some aspects of quantitative analysis and correction of radiation damage. *Acta Crystallogr D* 62:96–101.
9. Wang J, Ealick SE (2004) Observation of time-resolved structural changes by linear interpolation of highly redundant X-ray diffraction data. *Acta Crystallogr D* 60:1579–1585.
10. Ravelli RB, Leiros HK, Pan B, Caffrey M, McSweeney S (2003) Specific radiation damage can be used to solve macromolecular crystal structures. *Structure* 11:217–224.
11. Ravelli RB, Nanao MH, Lovering A, White S, McSweeney S (2005) Phasing in the presence of radiation damage. *J Synchrotron Radiat* 12:276–284.
12. Nanao MH, Sheldrick GM, Ravelli RB (2005) Improving radiation-damage substructures for RIP. *Acta Crystallogr D* 61:1227–1237.
13. Evans G, Polentarutti M, Djinovic Carugo K, Bricogne G (2003) SAD phasing with triiodide, softer X-rays and some help from radiation damage. *Acta Crystallogr D* 59:1429–1434.
14. Banumathi S, Zwart PH, Ramagopal UA, Dauter M, Dauter Z (2004) Structural effects of radiation damage and its potential for phasing. *Acta Crystallogr D* 60:1085–1093.
15. Ramagopal UA, Dauter Z, Thirumuruhan R, Fedorov E, Almo SC (2005) Radiation-induced site-specific damage of mercury derivatives: Phasing and implications. *Acta Crystallogr D* 61:1289–1298.
16. Schiltz M, Bricogne G (2007) Modelling and refining site-specific radiation damage in SAD/MAD phasing. *J Synchrotron Radiat* 14:34–42.
17. Smith NV, Himpsel FJ, Eastman DE, Farge Y, eds. (1983) *Handbook on Synchrotron Radiation* (North-Holland, New York), 1b, pp 917–921.
18. Nave C, Hill MA (2005) Will reduced radiation damage occur with very small crystals? *J Synchrotron Radiat* 12:299–303.
19. Cowan JA, Nave C (2008) The optimum conditions to collect X-ray data from very small samples. *J Synchrotron Radiat* 15:458–462.
20. Fischetti RF, et al. (2009) Mini-beam collimator enables micro-crystallography experiments on standard beamlines. *J Synchrotron Radiat* 16:217–225.
21. Flot D, et al. (2010) The ID23-2 structural biology microfocus beamline at the ESRF. *J Synchrotron Radiat* 17:107–118.
22. Riekel C (2004) Recent developments in microdiffraction on protein crystals. *J Synchrotron Radiat* 11:4–6.
23. Thomas SJ (1994) Factors affecting penumbral shape and 3D dose distributions in stereotactic radiotherapy. *Phys Med Biol* 39:761–771.
24. Paithankar KS, Owen RL, Garman EF (2009) Absorbed dose calculations for macromolecular crystals: Improvements to RADDOSE. *J Synchrotron Radiat* 16:152–162.
25. Owen RL, Rudino-Pinera E, Garman EF (2006) Experimental determination of the radiation dose limit for cryocooled protein crystals. *Proc Natl Acad Sci USA* 103:4912–4917.
26. Riekel C, Burghammer M, Schertler G (2005) Protein crystallography microdiffraction. *Curr Opin Struct Biol* 15:556–562.
27. Glaeser R, et al. (2000) Characterization of conditions required for X-Ray diffraction experiments with protein microcrystals. *Biophys J* 78:3178–3185.
28. Boutet S, Robinson IK (2006) Radiation driven collapse of protein crystals. *J Synchrotron Radiat* 13:1–7.
29. Rasmussen SG, et al. (2007) Crystal structure of the human beta2 adrenergic G-protein-coupled receptor. *Nature* 450:383–387.
30. Finfrock YZ, et al. (2010) Spatial dependence and mitigation of radiation damage by a line-focus mini-beam. *Acta Crystallogr D* 66:1287–1294.
31. Stern EA, et al. (2009) Reducing radiation damage in macromolecular crystals at synchrotron sources. *Acta Crystallogr D* 65:366–374.
32. Paithankar KS, Garman EF (2010) Know your dose: RADDOSE. *Acta Crystallogr D* 66:381–388.
33. Fischetti RF, et al. (2007) Optical performance of the GM/CA-CAT canted undulator beamlines for protein crystallography. *AIP Conference Proceedings: Ninth International Conference on Synchrotron Radiation Instrumentation*, eds J-Y Choi and S Rah 879 (Springer, New York), pp 754–757.
34. Kirz J, Jacobsen C, Howells M (1999) Soft X-ray microscopes and their biological applications. *Q Rev Biophys* 28:33–130.
35. Xu S, et al. (2010) Micro-crystallography developments at GM/CA-CAT at the APS. *AIP Conference Proceedings: Tenth International Conference on Synchrotron Radiation Instrumentation*, 1234 (Springer, New York), pp 905–908.

# Supporting Information

Sanishvili et al. 10.1073/pnas.1017701108

## SI Text

**X-Ray Beam Properties.** The radiation damage experiments were performed on beamline 23ID-B of the Advanced Photon Source at Argonne National Laboratory. This beamline is one of a pair of rapidly and fully tunable dual-canted undulator beamlines. The general layout of the beamline includes a 62-pole undulator with a 3.3-cm magnetic period; white-beam slits; a cryogenically cooled, constant-exit-height, double-crystal monochromator; a pair of plane horizontally deflecting mirrors to further separate the two canted beams; monochromatic beam slits; "bimorph" focusing mirrors arranged in a Kirkpatrick–Baez geometry; monochromatic beam attenuators; and an endstation goniometer support. The details of the layout of the beamline optics have been described (1).

The goniometer support stand has two independent motorized platforms that we refer to as the "beam delivery support" and the "goniometer support." The beam delivery support carries the downstream end of the evacuated beam pipe, as well as the motorized pitch and yaw motions for the beam conditioning/monitoring components. These include a quadrant-diode beam position monitor (2), beam-defining slits, a fast timing shutter, and an $I_0$ intensity monitor. A high-resolution microscope, referred to as an on-axis visualizer, has a hole through the optical axis, allowing the X-ray and visual optical axes to coincide, providing a parallax-free view of the sample. A minibeam collimator allows users to condition the beam with a 5-, 10-, or 20-μm beam-defining pinhole or a 300-μm scatter guard combined with beam-defining slits (3).

The wide range of beam sizes used in these experiments required two different optical configurations (Fig. S1). For beam sizes larger than 5 μm, the mirrors focused the beam to $25 \times 120$ μm$^2$ [vertical × horizontal (V × H); full-width at half-maximum (FWHM)] at the sample position. Beams with nearly circular cross-sections were achieved by using the minibeam collimators developed in-house (3) (Fig. S1*A* and Table S1). Beam sizes smaller than 5 μm required different X-ray optics. For these experiments, the beamline focusing mirrors were removed from the beam path, and a circular Fresnel zone plate (FZP) optic (4) was mounted on the beam delivery support (Fig. S1*B*). Different FZPs were used for the experiments at 15.1 keV (5) and 18.5 keV (Xradia, Inc.) (Table S2).

The FZP was mounted on a New Focus Manual Fiber Positioner (model 9051, Newport Corp.), and the central stop was mounted on a New Focus Motorized Fiber Positioner (model 8051, Newport Corp.), providing remote relative alignment of the FZP and central stop. Both of these were mounted on a common support attached to a pair of linear stages (model MFN25PP, Newport Corp.) configured to provide XY motion of the FZP and central stop in a plane perpendicular to the beam direction. The assembly was attached to a rail allowing manual adjustment of the position of the FZP and central stop along the beam direction. The rail was attached to the beam delivery support. Each zone plate was positioned at the theoretical focal distance for the target energy (15.1 and 18.5 keV). The FZP was centered on the beam and oriented roughly perpendicular to the beam propagation direction. A 40-μm-diameter central stop was positioned approximately 40 mm upstream of the FZP and was centered on the FZP. A minibeam collimator with a 20-μm aperture was used as the order-sorting aperture (OSA).

The X-ray beam source size was $630 \times 30$ μm$^2$ (H × V, FWHM), and with FZP no. 1 the demagnification ratio was approximately 76:1 with the FZP positioned at the theoretical focal length from the sample position. Thus, one could achieve a submicron vertical focus at the sample position. Focusing was achieved by recording the beam size at several energies over a small range to determine the energy of minimum beam size in the vertical direction. This defined the energy used for the experiments, namely, 15.10 keV for FZP no. 1 and 18.50 keV for FZP no. 2. To achieve a 1-μm beam in the horizontal direction, the white-beam slits (Table S2) were used to provide a secondary source point with an approximately 38:1 demagnification ratio. Closing the horizontal aperture to 0.04 mm (from a typical size of 2.00 mm) allowed the 15.1-keV beam to be focused to 1.2 μm by rotating the FZP about its vertical axis. The vertical beam size was increased to provide a circular beam profile by rotating the FZP about its horizontal axis (6). The focal length was significantly shorter for FZP no. 2 than for FZP no. 1, providing a greater demagnification ratio and a submicron focused beam with FZP no. 2. Beam sizes below 5 μm at the sample position were achieved by translating the FZP assembly upstream, resulting in a focal position slightly upstream of the sample.

The beam size at the sample position was determined by scanning a silicon knife edge coated with a 500-Å layer of platinum (5) through the beam while recording the Pt $L_\alpha$ and $L_\beta$ fluorescence with a silicon drift detector (Model AXAS-M1-H80-139V, Ketek, GmbH). The data were fit with a Gauss error function, which was differentiated to provide the best-fit Gaussian profile of the beam (Table S1 and Fig. S2). The beam profile is well described by a Gaussian function. The smallest beam size used in these experiments was achieved with FZP no. 2 focused at the sample position with an X-ray energy of 18.5 keV. The measured beam size was $0.88 \times 0.80$ μm$^2$ (H × V, FWHM).

The X-ray beam intensity at the sample position was measured by converting the photocurrent from an ion chamber (10-mm gap, 60-mm path length, $N_2$ gas, 2500 V) operating in the plateau region. The photocurrent conversion factor for the 15.1- and 18.5-keV X-rays was calculated based on the measured capture length of the ion chamber (60.32 mm), the density of nitrogen gas at STP, a binding energy of 33.8 eV, and the photoelectric cross-section for nitrogen obtained from a tabulation (http://csrri.iit.edu/periodic-table.html) based on accepted values (7).

The intensity was measured for each beam size at both 15.1 keV and 18.5 keV (Table S1). The ion chamber measurements were used to calibrate the current from a PIN diode and an "active" beamstop (8), which could be used to monitor beam intensity during the experiment.

The convergence angle was measured to be approximately 100 μrad (FWHM) for the minibeams (3) and was estimated from the zone plate diameter and focal distance to be approximately 320 and 660 μrad for the two zone plates used in these experiments (Table S2).

**Goniometry.** The beam size on typical protein crystallography beamlines ranges from tens to hundreds of microns. A common requirement for the sample goniometry is that the stability, accuracy, reproducibility, and sphere-of-confusion (SOC) should be 10% of the beam or sample size (8). Similar requirements apply to the X-ray beam position to ensure that the intersection of the sample and the beam is maintained. These standards are met for typical operations of beamline 23-ID-B with beam sizes down to 10 μm. However, applying the same standards to experiments with a 1-μm beam required better than 0.1-μm precision in most of the parameters above. To achieve these requirements, direct-reading linear optical encoders (5- to 50-nm resolution) were

added to the beam delivery and goniometer support motions. The goniometer had three components: (*i*) an air-bearing rotation axis (ABR100, AreoTech, Inc.), (*ii*) a pair of XY stages mounted on the rotation surface, and (*iii*) a nano-positioning goniometer head mounted on the XY stages. The rotation axis was oriented in a horizontal plane and was perpendicular to the beam direction (parallel to the X-ray beam polarization vector). An SOC of approximately 1.0 μm was achieved by disassembling and carefully realigning the components of the air-bearing rotation axis during reassembly and by designing and fabricating a membrane-based XY positioner (8). For the experiments described herein, diffraction images were recorded over 1.0° of sample rotation so the 1.0-μm SOC was sufficient. To achieve the required 0.1-μm precision in sample translation, we built a nano-positioning goniometer head. Two linear stages with 5-nm direct optical encoding (PP-30, MICOS USA, LLC) and a high-precision ball slide (HPM-1, DEL-TRON Precision, Inc.) provided motions in a plane perpendicular to the beam direction (6). The goniometer head was used to position the knife edge for recording the beam profiles described above and to position samples for studies of the spatial extent of radiation damage.

**Crystallization.** Chicken egg-white lysozyme crystals in the tetragonal form (space group $P4_32_12$) were used for all experiments. Crystals were grown by hanging-drop vapor diffusion as described earlier (9). When crystals did not grow spontaneously within 17–20 h of setup, the drops were streak-seeded. An acupuncture needle of 5- to 10-μm diameter was loaded with microcrystals by plunging it into a large crystal. Excess seeds were washed off by passing the needle through the well solution. Then, the crystallization drops were seeded by streaking the needle through the drops. Twelve drops were seeded successively with a single needle-load to achieve gradual dilution of seeds, resulting in a varying number and size of crystals. Crystallization solutions contained 28–30% glycerol, which acted as a cryoprotectant. Crystals were harvested with MiTeGen micromounts (MiTeGen, LLC) directly from crystallization drops and vitrified by plunging them into the liquid nitrogen.

**Measurement and Analysis of Diffraction Images.** Various metrics have been used in studies of X-ray radiation-induced damage of macromolecular crystals. These include changes in refined crystal mosaicity, unit cell dimensions, Wilson B factor, merging scale factor, total diffracted intensity, merging $\chi^2$ values, $I/\sigma_I$, merging R factors, minimum *d*-spacing, molecular structure, and magnitude of anomalous signal (10–32). Investigation of the spatial extent of damage required probe measurements that result in a minimum exposure to a minimum crystal volume but provide sufficient data for analysis. A narrow angular rotation about the horizontal omega axis was essential in probe measurements to map damage in the vertical direction without significant overlap of irradiated volumes. Thus, we excluded metrics that would require a complete, or nearly complete, diffraction dataset. The sum of integrated intensities of all Bragg reflections on each probe image was chosen as the metric for several reasons. First, a sufficient number of reflections for analysis could be obtained from a narrow angular swath of data. Second, the use of summed integrated intensities as a metric avoided the need for accurate estimates of the partiality of Bragg reflections and the errors of individual intensities ($\sigma_I$). Third, reflections that became impossible to integrate because of radiation damage during the experiment appropriately contributed zero to the sum of integrated intensities.

Experimental parameters were selected to balance the conflicting needs for a maximum number of integrated diffraction intensities for analysis and, in the spatial extent of damage experiments, minimum damage from probe measurements and minimum volume of crystal swept by the beam in each probe measurement. Control images were recorded using angular widths in the range 0.1–2.0°. The optimal balance was obtained with a single image of width 1.0°, which was used for experiments on both the dependence of damage on beam size and the spatial extent of damage. Exposure time and beam attenuation were adjusted so that the CCD detector used to record diffraction images (MAR*Mosaic* 300) had no overloaded pixels in the initial diffraction images.

Diffraction images were indexed and integrated using HKL2000 (33). The same initial crystal orientation matrix was used for indexing all images collected in each experiment. Intensity estimates from two-dimensional profile fitting were analyzed with an in-house program that grouped individual reflections by Miller indices and by radiation exposure (number of burns). Reflections having negative intensities and those with $I/\sigma_I < 2$ were excluded. As damage progressed and crystal mosaicity increased, exclusion of partially recorded reflections from the total diffracted intensity values would lead to an overestimation of decay. Therefore, both fully and partially recorded reflections were included. Furthermore, inclusion of both fully and partially recorded reflections significantly increased the number of observations and also the statistical validity of the analysis.

Several approaches to analyzing the integrated intensities were explored to identify one that provided a reliable, statistically significant measure of radiation damage. Intensities were monitored for individual reflections, for reflections binned by d-spacing, and as the sum of all reflection intensities in a probe measurement. For analyses using reflections binned by d-spacing, bin boundaries were established for the first image in each experiment and enforced for all subsequent ones. Statistical noise was a problem for analyses of individual reflection intensities and of binned data. Decay of individual reflection intensities was sensitive to the difficulty of obtaining accurate crystal orientation, unit cell dimensions, crystal mosaicity, and estimates of reflection partiality from a single 1° diffraction image, and to damage-induced changes in these parameters. Binning of reflections into resolution shells, whether the bins had equal volume in reciprocal space or equal numbers of integrated intensities with $I > 2\sigma_I$, led to erratic behavior in higher-resolution shells, which had fewer reflections as the radiation dose increased. Therefore, decay was monitored as the change in total integrated intensity ($I$) for reflections with $I > 2\sigma_I$, including all partially and fully recorded reflections. In each experiment, the total diffracted intensity was normalized to the value of the initial measurement at each position on the crystal.

**Radiation Damage as a Function of Beam Size.** For each beam size, repeated 1° diffraction images were recorded from a single spot on the crystal using an identical omega start, exposure time, and beam attenuation until the total diffracted intensity decayed by at least 10–20%. Data recorded with the 5.35-, 8.85-, and 15.6-μm beams were measured from two crystals that were translated after the series of images for each beam size (30-μm translation between measurements with the smaller beam sizes, and 40–50 μm between measurements with the larger beam sizes). Separate crystals were used to record data with the 0.84-, 1.81-, and 2.71-μm beams. Data were averaged from two to three experiments for each beam size.

The dose per diffraction image was calculated with RADDOSE (34) using the measured properties of the crystal (dimensions and chemical composition) and the beam (flux, size, attenuation, and exposure time). The normalized total diffracted intensity was plotted as a function of calculated dose and fit to a straight line for each beam size (Fig. 1*A*). The average slope for each of the experiments with 0.84-, 1.81-, 2.71-, 5.35-, 8.85-, and 15.6-μm beams was corrected for the volume swept by the 1° rotation of the crystal, as follows. For an X-ray exposure with fixed angle ($\Delta\theta = 0$), the volume illuminated by the beam is

$V_0 = \pi r_w r_h L$, where $r_w$ is the half-width and $r_h$ the half-height of the beam, and $L$ is the crystal thickness. When the crystal is rotated through an angle $\Delta\theta$ (from $-\Delta\theta/2$ to $+\Delta\theta/2$ about the starting position), the illuminated volume increases by an additional term $\Delta V = (r_w L^2)\tan(\Delta\theta/2)$. The dose was calculated using RADDOSE with the volume $V_0$ for the fixed-angle illumination, and thus it is an overestimate of the true dose. The experimental rate of decay was corrected for the increase in exposed volume due to crystal rotation as the ratio of $V_0/(V_0 + \Delta V) = 1/(1 + (L/\pi r_h)\tan(\Delta\theta/2))$ and was renormalized to the rate for the largest beam size. This simple correction results in an underestimate of the true dose because it treats the total illuminated volume $(V_0 + \Delta V)$ as continuously illuminated. Thus, the uncorrected and corrected slopes represent boundaries on the true slope. The raw experimental slope of intensity loss vs. calculated dose and the slope values corrected for the swept volume are listed in Table S3; the corrected values are plotted in Fig. 1*B*. For the 30- to 50-μm crystal thicknesses used in these experiments, the swept-volume correction is substantial for only the smallest beam (vertical dimension of 0.80 μm FWHM), where $\Delta V$ is 21% of $V_0$ for crystal thickness 30 μm and 35% of $V_0$ for crystal thickness 50 μm. With the larger beams, $\Delta V$ is 2–10% of $V_0$, dependent on crystal thickness.

**Spatial Extent of Radiation Damage.** Diffraction images were recorded in a probe-burn-probe mode with burn and probe positions offset in the horizontal or vertical direction by a specified distance (Fig. 2). The general sequence was to record a probe image, then to subject the crystal to a burn dose at a defined distance from the probe position, and then to rerecord an image at the probe position. The burn-probe sequence was repeated until the total diffracted intensity at the probe position decayed by more than 50%, which typically required four to six burn/probe cycles. Probe points for each burn spot were defined in steps of $1.00 \pm 0.05$ μm in directions parallel (horizontal) or perpendicular (vertical) to the polarization direction. All probe images in an experiment were recorded with identical values for parameters such as omega start, rotation width, beam attenuation, and exposure time. Each burn dose comprised 10 successive diffraction images with the same parameters as the probe images. Thus, the probe exposure was 1/10 of the burn exposure.

Two protocols were used for accumulating the patterns of probe positions. In the "contiguous-probe" protocol (Fig. 2*A*), an initial probe image was recorded for all positions of the desired pattern; the crystal was then translated back to the origin and subjected to a burn dose; diffraction images were recorded again at all probe positions, and the process was repeated four to six times. In the "isolated-probe" protocol (Fig. 2*B*), the pattern was composed from individual burn/probe pairs in which a spatially isolated probe-$(\text{burn-probe})_n$ sequence was performed for each distance. Each pair of probe/burn positions was separated from all other such pairs by 12–20 μm, based on preliminary experiments demonstrating that radiation damage did not extend beyond 4–6 μm. The isolated-probe protocol, in combination with correction for the damage by the probe beam (see below, Fig. S4), resulted in artifact-free, direct measurement of the spatial extent of radiation damage profiles (Fig. S3).

All experiments were performed with a 1-μm beam using exposure times of 4–7 s with no beam attenuation. Crystal dimensions were 50–300 μm perpendicular to the X-ray beam. Because crystals were large relative to the beam size and the length scale of the experiments, several probe-burn-probe patterns were recorded from different regions of each crystal. Most crystals were 50–60 μm thick along the beam. We also used one thick crystal (140 μm). Crystal height and thickness were distinct variables in these experiments because all diffraction images recorded from each crystal were taken over 1° of rotation from an identical initial rotation setting. The diffraction limits varied from 1.23 to 1.8 Å. Refined mosaicities among the crystals and from several positions within each crystal were 0.14–0.40°.

A total of 618–2,300 integrated intensities were used in the analysis of initial probe measurements, and at the end of the probe-burn-probe series, the total dropped to 340–1,100 integrated intensities due to accumulated decay. Data were measured from a total of six crystals at 15.1 keV and averaged from seven and eight experiments in horizontal and vertical patterns, respectively. At 18.5 keV, two crystals were used, providing eight measurements in horizontal patterns and six in vertical patterns.

For each probe position, radiation damage was monitored as the fractional decay of the total diffracted intensity relative to the total intensity in the initial probe image before the burn position was subjected to any dose. The fractional loss ($\Delta_i$) in total diffracted intensity ($I$) was calculated for diffraction images as

$$\Delta_i = 1 - I_i/I_1, \qquad \text{[S1]}$$

where $I_i$ and $I_1$ are the total intensities of the $i$th and initial images at the probe position, respectively.

Diffraction images recorded at the burn position for each dose were used to monitor damage at the burn position and as experiment controls. Any experiments with discontinuities in the decay curves were excluded from analysis. The few such cases indicated an experimental problem such as beam drift, intensity fluctuations, or exposure inconsistency. Images in the initial burn series of each experiment were also used to correct decay curves for radiation damage caused by measurement of the probe images themselves. For the 10 images of the first burn series, the plot of intensity loss vs. image number (proportional to dose) was approximately linear (Fig. S4). In each experiment, the fractional intensity loss per image was taken as a measure of probe damage and subtracted from $\Delta_i$ to obtain a corrected fractional decay value.

**Monte Carlo Simulations with CASINO.** The program CASINO (http://www.gel.usherbrooke.ca/casino/What.html) was used to perform Monte Carlo simulations of photoelectron trajectories (Fig. 5). Input parameters included the atomic composition and density of the protein crystal (35). The electron energy was equal to the X-ray energy minus the 700-eV average electron binding energy for a typical protein atom. The number of electrons in the simulations was chosen to be proportional to the probability of ejection within azimuth (tilt) angles between 0° and 20° for the 0° beam angle simulation, 20° and 45° for the 30° beam angle simulation, and 45° and 75° for the 60° beam angle simulation. The number of electrons used in the simulation was 2,000 for the 0° tilt angle case. The trajectories shown represent all trajectories distributed isotropically around the polarization vector for the given azimuth angle range. The beam diameter was set to 1 μm.


1. Fischetti RF, et al. (2007) Optical performance of the GM/CA-CAT canted undulator beamlines for protein crystallography. *AIP Conference Proceedings: Ninth International Conference on Synchrotron Radiation Instrumentation*, eds Choi J-Y, Rah S (Springer, New York), Vol 879, pp 754–757.
2. Alkire RW, Rosenbaum G, Evans G (2000) Design of a vacuum-compatible high-precision monochromatic beam-position monitor for use with synchrotron radiation from 5 to 25 keV. *J Synchrotron Radiat* 7:61–68.
3. Fischetti RF, *et al.* (2009) Mini-beam collimator enables micro-crystallography experiments on standard beamlines. *J Synchrotron Radiat* 16:217–225.
4. Kirz J, Jacobsen C, Howells M (1999) Soft X-ray microscopes and their biological appliations. *Q Rev Biophys* 28:33–130.
5. Yun W, et al. (1999) Nanometer focusing of hard x rays by phase zone plates. *Rev Sci Instrum* 70:2238–2241.
6. Yoder DW, et al. (2010) One-micron beams for macromolecular crystallography at GM/CA-CAT. *AIP Conference Proceedings: Tenth International Conference on Synchrotron Radiation Instrumentation* (Springer, New York), Vol 1234, pp 413–416.

7. McMaster WH, Del Grande NK, Mallett JH, Hubbell JH (1969) *Compilation of X-ray Cross Sections* (Lawrence Livermore National Laboratory Report, US Department of Commerce, Livermore, CA), Vol UCRL-50174, Section II, Revision I.
8. Xu S, et al. (2010) Micro-crystallography developments at GM/CA-CAT at the APS. *AIP Conference Proceedings: Tenth International Conference on Synchrotron Radiation Instrumentation* (Springer, New York), Vol 1234, pp 897–902.
9. Sanishvili R, et al. (2008) A 7 μm mini-beam improves diffraction data from small or imperfect crystals of macromolecules. *Acta Crystallogr D* 64:425–435.
10. Muller R, Weckert E, Zellner J, Drakopoulos M (2002) Investigation of radiation-dose-induced changes in organic light-atom crystals by accurate d-spacing measurements. *J Synchrotron Radiat* 9:368–374.
11. Ravelli RB, McSweeney SM (2000) The "fingerprint" that X-rays can leave on structures. *Structure* 8:315–328.
12. Meents A, et al. (2007) Reduction of X-ray-induced radiation damage of macromolecular crystals by data collection at 15 K: A systematic study. *Acta Crystallogr D* 63:302–309.
13. Leiros HK, Timmins J, Ravelli RB, McSweeney SM (2006) Is radiation damage dependent on the dose rate used during macromolecular crystallography data collection? *Acta Crystallogr D* 62:125–132.
14. Shimizu N, Hirata K, Hasegawa K, Ueno G, Yamamoto M (2007) Dose dependence of radiation damage for protein crystals studied at various X-ray energies. *J Synchrotron Radiat* 14:4–10.
15. Kmetko J, Husseini NS, Naides M, Kalinin Y, Thorne RE (2006) Quantifying X-ray radiation damage in protein crystals at cryogenic temperatures. *Acta Crystallogr D* 62:1030–1038.
16. Burmeister WP (2000) Structural changes in a cryo-cooled protein crystal owing to radiation damage. *Acta Crystallogr D* 56:328–341.
17. Owen RL, Rudino-Pinera E, Garman EF (2006) Experimental determination of the radiation dose limit for cryocooled protein crystals. *Proc Natl Acad Sci USA* 103:4912–4917.
18. Teng TY, Moffat K (2000) Primary radiation damage of protein crystals by an intense synchrotron X-ray beam. *J Synchrotron Radiat* 7:313–317.
19. Teng TY, Moffat K (2002) Radiation damage of protein crystals at cryogenic temperatures between 40 K and 150 K. *J Synchrotron Radiat* 9:198–201.
20. Ramagopal UA, Dauter Z, Thirumuruhan R, Fedorov E, Almo SC (2005) Radiation-induced site-specific damage of mercury derivatives: Phasing and implications. *Acta Crystallogr D* 61:1289–1298.
21. Chinte U, et al. (2007) Cryogenic (<20 K) helium cooling mitigates radiation damage to protein crystals. *Acta Crystallogr D* 63:486–492.
22. Murray J, Garman E (2002) Investigation of possible free-radical scavengers and metrics for radiation damage in protein cryocrystallography. *J Synchrotron Radiat* 9:347–354.
23. Weik M, et al. (2001) Specific protein dynamics near the solvent glass transition assayed by radiation-induced structural changes. *Protein Sci* 10:1953–1961.
24. Diederichs K (2006) Some aspects of quantitative analysis and correction of radiation damage. *Acta Crystallogr D* 62:96–101.
25. Sliz P, Harrison SC, Rosenbaum G (2003) How does radiation damage in protein crystals depend on X-ray dose? *Structure* 11:13–19.
26. Weiss MS, Panjikar S, Mueller-Dieckmann C, Tucker PA (2005) On the influence of the incident photon energy on the radiation damage in crystalline biological samples. *J Synchrotron Radiat* 12:304–309.
27. Banumathi S, Zwart PH, Ramagopal UA, Dauter M, Dauter Z (2004) Structural effects of radiation damage and its potential for phasing. *Acta Crystallogr D* 60:1085–1093.
28. Evans G, Polentarutti M, Djinovic Carugo K, Bricogne G (2003) SAD phasing with triiodide, softer X-rays and some help from radiation damage. *Acta Crystallogr D* 59:1429–1434.
29. Ravelli RB, Theveneau P, McSweeney S, Caffrey M (2002) Unit-cell volume change as a metric of radiation damage in crystals of macromolecules. *J Synchrotron Radiat* 9:355–360.
30. Yonath A, et al. (1998) Crystallographic studies on the ribosome, a large macromolecular assembly exhibiting severe nonisomorphism, extreme beam sensitivity and no internal symmetry. *Acta Crystallogr A* 54:945–955.
31. Zwart PH, Banumathi S, Dauter M, Dauter Z (2004) Radiation-damage-induced phasing with anomalous scattering: Substructure solution and phasing. *Acta Crystallogr D* 60:1958–1963.
32. Ravelli RB, Nanao MH, Lovering A, White S, McSweeney S (2005) Phasing in the presence of radiation damage. *J Synchrotron Radiat* 12:276–284.
33. Otwinowski Z, Minor W (1997) Processing of X-ray diffraction data collected in oscillation mode. *Methods Enzymol* 276:307–326.
34. Paithankar KS, Owen RL, Garman EF (2009) Absorbed dose calculations for macromolecular crystals: Improvements to RADDOSE. *J Synchrotron Radiat* 16:152–162.
35. Nave C, Hill MA (2005) Will reduced radiation damage occur with very small crystals? *J Synchrotron Radiat* 12:299–303.


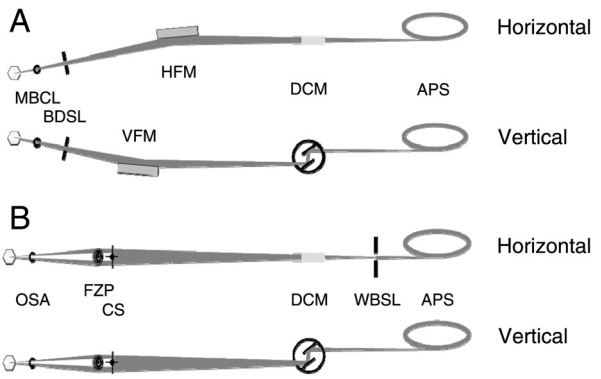


**Fig. S1.** Schematic diagrams of beamline optics. The APS undulator source is at the right and the sample at the left of each diagram. (*A*) Beamline optics for beam sizes of 5 μm or larger. The beam from the double-crystal monochromator (DCM) is focused by horizontal (HFM) and vertical (VFM) mirrors and passes through beam-defining slits (BDSL) and a minibeam collimator (MBCL), which contains the beam-defining aperture. (*B*) Beamline optics for beam sizes less than 5 μm. The beam from the DCM is focused with an FZP with central stop (CS) and OSA to produce a beam with cross-section down to 1.2 μm at 15.1 keV with FZP no. 1 and 0.84 μm at 18.5 keV with FZP no. 2.

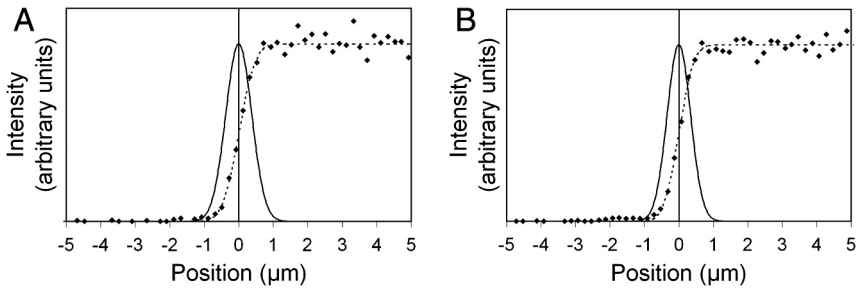


**Fig. S2.** Typical beam profiles measured at 18.5 keV by recording the fluorescence from a 500-Å-thick platinum evaporate on a silicon knife edge. A Gauss error function (dashed line) was fit to the data points (dots). The Gaussian profile (derivative of the Gauss error function) is shown as a solid line. (*A*) Horizontal profile, FWHM $= 0.88 \pm 0.02$ μm. (*B*) Vertical profile, FWHM $= 0.80 \pm 0.08$ μm. The beam profile is well described by a Gaussian function.

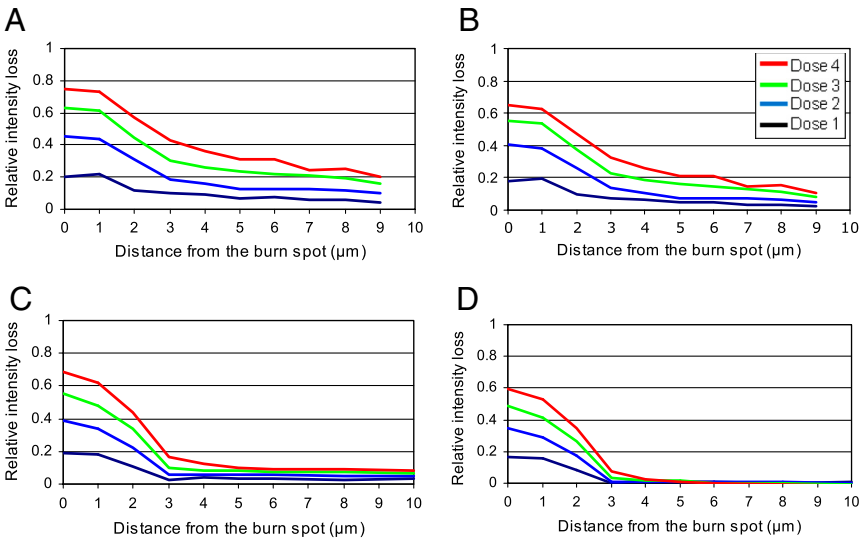


**Fig. S3.** Normalized total integrated intensity loss as a function of distance from the center of the burn beam. (*A*) Observed decay for the contiguous-probe data collection protocol. Note that damage was observed even at the greatest distance from the burn-beam center. (*B*) Decay for the contiguous-probe protocol after correction for damage caused by the probe beam. (*C*) Observed decay for the isolated-probe data collection protocol. (*D*) Decay for the isolated-probe protocol after correction for probe-beam damage. The combination of the isolated-probe data collection protocol and correction for probe-beam damage removes artifacts that mask the range of damage caused by the burn dose.

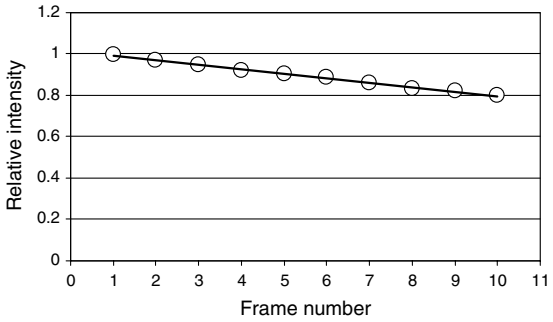


**Fig. S4.** Normalized total integrated intensity for a typical burn series. The probe-beam dose was equivalent to that of a single exposure of the 10-exposure burn series, and, therefore, corresponded to 1/10 of the burn dose. The slope of the integrated intensity as a function of exposure number in the initial burn was used to correct decay curves for radiation damage induced by the probe beam.

**Table S1. Beam properties for all beam sizes used at 15.1 keV and 18.5 keV**

| Beam width (FWHM, μm) | Beam height (FWHM, μm) | Average beam size (FWHM, μm) | Flux, photons/s | Average peak flux density, photons per s/mm$^2$ |
|---|---|---|---|---|
| 15.1 keV | | | | |
| 1.16 (4)* | 1.18 (1) | 1.17 | $1.93 \times 10^9$ | $1.80 \times 10^{15}$ |
| 18.5 keV | | | | |
| 0.88 (2) | 0.80 (8) | 0.84 | $1.25 \times 10^9$ | $2.29 \times 10^{15}$ |
| 1.79 (6) | 1.82 (17) | 1.81 | $7.17 \times 10^8$ | $2.80 \times 10^{14}$ |
| 2.71 (5) | 2.71 (5) | 2.71 | $2.65 \times 10^9$ | $4.60 \times 10^{14}$ |
| 5.6 (2) | 5.1 (2) | 5.35 | $2.77 \times 10^{10}$ | $1.24 \times 10^{15}$ |
| 9.3 (2) | 8.4 (4) | 8.85 | $8.01 \times 10^{10}$ | $1.31 \times 10^{15}$ |
| 16.6 (2) | 14.6 (1) | 15.6 | $2.04 \times 10^{11}$ | $1.07 \times 10^{15}$ |

*Standard deviations are in parentheses.

**Table S2. Optical parameters for FZP optics**

| Properties | FZP no. 1 | FZP no. 2 |
|---|---|---|
| Source position*, m | −1.250 | −1.250 |
| Monochromator position*, m | 28.900 | 28.900 |
| White-beam horizontal slit*, m | 27.314 | 27.314 |
| FZP position*, m | 55.457 | 55.718 |
| Focal position*, m | 56.200 | 56.200 |
| Focal distance, m | 0.743 | 0.482 |
| Horizontal magnification | 1/37.9 | 1/58.9 |
| Vertical magnification | 1/76.3 | 1/118.2 |
| OD[†], μm | 240 | 320 |
| $N$[‡] | 240 | 800 |
| $\Delta R_N$[§], μm | 0.25 | 0.10 |
| Energy, keV | 15.10 | 18.50 |
| Wavelength, Å | 0.821 | 0.670 |
| Focal length[¶], m | 0.731 | 0.477 |
| Beam convergence angle, μrad | 320 | 660 |

*Positions are relative to the center of the straight section.
[†]OD, FZP outer diameter.
[‡]$N$, number of rings.
[§]$\Delta R_N$, width of the outermost ring.
[¶]Focal length ($f = \mathrm{OD} \times \Delta R_N/\mathrm{wavelength}$) is calculated for each FZP at the specified energy.

**Table S3. Correction for swept volume in decay vs. beam size experiment**

| Beam size, μm | Normalized experimental slope of intensity loss vs. dose | Normalized experimental slope of intensity loss vs. dose corrected for swept volume* |
|---|---|---|
| 0.84 | 0.28 | 0.35 |
| 1.81 | 0.41 | 0.45 |
| 2.71 | 0.60 | 0.64 |
| 5.35 | 0.78 | 0.80 |
| 8.85 | 0.92 | 0.93 |
| 15.6 | 1.00 | 1.00 |

*For crystal thicknesses varying from 30–50 μm.